Materials Advances

ROYAL SOCIETY OF CHEMISTRY

PAPER

View Article Online
View Journal

Cite this: DOI: 10.1039/d5ma01336d

DFT-driven insights into the electronic, magnetic, and transport properties of a 2D Nb_3C_2 MXene for high-performance Li-ion batteries

Samia Tahira,[a] Safwara Siddiqua,[a] Fouzia Perveen Malik *[a] and Hummera Rafique[b]

Received 17th November 2025,
Accepted 4th April 2026

DOI: 10.1039/d5ma01336d

rsc.li/materials-advances

'MXenes', two-dimensional materials, have attained significant attention for their outstanding characteristics inherent to their nanostructures. However, to date, the Nb_3C_2 MXene, particularly in Cr-doped form, has not been theoretically explored for Li-ion battery applications. In this work, first-principles calculations were performed to explore the structural, electronic, magnetic, and transport properties of newly designed pristine Nb_3C_2 and Cr-doped Nb_3C_2, along with their energy storage potential, using the FP-LAPW approach. Both structures are dynamically and thermally stable, as confirmed from phonon dispersion and AIMD simulations. Electronic properties, including the band structure and density of states, indicate metallic behavior in both structures with an indirect band gap, fulfilling a key requirement for electrode materials in energy storage systems. Pristine Nb_3C_2 exhibits an essentially non-magnetic ground state, while Cr-doped Nb_3C_2 exhibits ferromagnetic behavior. Theoretical capacities of 169 mAh g^{-1} for pristine Nb_3C_2 and 280 mAh g^{-1} for Cr-doped Nb_3C_2 were obtained, indicating a substantial enhancement upon Cr doping and exceeding that of pristine Nb_2C (170 mAh g^{-1}) reported in the literature. The predicted electrochemical properties unveil that both pristine and Cr-doped Nb_3C_2 possess favorable open-circuit voltages within the desirable range for anode materials, along with high electronic conductivity and improved gravimetric capacity. Furthermore, transport property analysis based on semi-classical Boltzmann theory highlights their promising thermoelectric behavior, complementing their electrochemical performance and providing a comprehensive evaluation of MXenes in energy storage devices.

1. Introduction

The successful synthesis and research on graphene have compelled scientists to explore more graphene-like 2D materials, both experimentally and theoretically, made of elements beyond carbon, such as phosphorene, hexagonal boron nitride (h-BN), and transition metal dichalcogenides. These materials possess unique properties, such as a high surface area-to-volume ratio and excellent electrical and thermal conductivity, making them promising candidates for use in supercapacitors and batteries.[1]

However, the performance of current batteries is insufficient to adequately satisfy the escalating demand for extensive energy storage. In order to address and comprehend this challenge, an immediate imperative arises to actively pursue novel materials that exhibit enhanced performance attributes within energy storage systems.[2] Recently, a new class of 2D materials known as MXenes have been drawing much interest because of their exceptional geometries and electronic topologies, *i.e.*, excellent conductivity, fast ion diffusion, and hydrophilic nature, which make them competent materials for storage systems.[3] MXenes are graphene-like layered 2D early transition metal carbides, nitrides, or carbonitrides that have been prepared by selectively etching the A layers from 3D MAX phases ($M_{n+1}AX_n$, where n ranges from 1 to 3), for example, M_2AX, M_3AX_2, and M_4AX_3, where M denotes a transition metal (*e.g.*, Ti, Nb, Mo, Ta, Sc, V, Zr, *etc.*); A is an element from group III-A or IV-A (Al, Si, or Ga); and X corresponds to carbides, nitrides, or carbonitrides.[4] Because the M–X bond is stronger than the M–A bond, the A atom can be selectively etched to yield 2D MXenes.[5]

A number of studies have been carried out on Nb_2C and Nb_4C_3 MXenes because of their potential use in energy storage devices, catalysis, and biomedical applications. Ghidiu *et al.* reported the synthesis and characterization of the Nb_4C_3 MXene obtained by selectively etching Nb_4AlC_3.[6] Shen *et al.* demonstrated the synthesis of the Nb_2C MXene and explored its electrochemical performance for supercapacitors.[7] Nishat *et al.* described the electrochemical performance of Nb_2C and Nb_2CO_2 for Na- and Li-ion batteries using an *ab initio* approach.[8] Although several studies have been conducted on

[a] *Materials Modelling Lab, School of Interdisciplinary Engineering & Science (SINES), National University of Sciences and Technology (NUST), Sector H-12, Islamabad 44000, Pakistan. E-mail: fouzia@sines.nust.edu.pk*
[b] *Department of Chemistry, University of Gujrat, Gujrat-50700, Pakistan*

Nb-based MXenes, such as Nb_2C and Nb_4C_3, studies on Nb_3C_2 remain limited. Furthermore, Cr doping in Nb_2C and Nb_4C_3 MXenes has not yet been explored.[6,7] In particular, a systematic investigation of their structural stability and electronic, magnetic, and electrochemical properties upon transition metal doping, especially with Cr, has not been explored. Hence, a detailed first-principles study is required to evaluate the potential of Cr-doped Nb_3C_2 MXenes for high-performance Li-ion battery applications.

Furthermore, niobium-based MXenes show superior performance as anode materials in Li-ion batteries compared to Ti-based MXenes, as reported in the literature.[9] Nb_3C_2 holds a different M/X ratio compared to other members of the MXene family, making it unique and influencing its layer thickness, electron density, surface chemistry, and mechanical strength, thereby positioning it as a promising and versatile candidate for future energy devices.[10] Due to its layered configuration, the Nb_3C_2 MXene possesses a relatively small interlayer spacing, which hinders the intercalation and deintercalation of Li^+ ions during battery operation.[11] To overcome this limitation, various dopant atoms have been introduced to expand the interlayer distance and investigate their influence on the electrocatalytic behavior of MXenes.[12] Doping not only increases the lattice parameters but also tunes the band gap and enhances the electrical conductivity, thereby improving the overall electrochemical performance of the material.[13]

In recent years, several studies have demonstrated that doping can effectively modify the interlayer spacing and surface chemistry of MXenes, thereby improving their electrochemical performance.[14] Among potential dopants, Cr is notable for its good electrical conductivity and ionic radius (0.62 Å), closely matching that of niobium (0.64 Å), making it a promising candidate for Nb_3C_2 MXene doping.[15]

Herein, a systematic first-principles investigation of pristine Nb_3C_2 and Cr-doped Nb_3C_2 MXenes is performed to explore their structural stability, electronic structure, magnetic behavior, transport properties, and electrochemical performance as potential anode materials for Li-ion batteries. Furthermore, the effect of Cr doping on the structural, electronic, and electrochemical properties of Nb_3C_2 is comprehensively examined.

The findings of this work provide valuable theoretical insights into the properties of the Nb_3C_2 MXene and highlight the potential of Cr doping to improve its electrochemical performance, thereby supporting future experimental investigations and the development of advanced MXene-based energy storage devices.

2. Computational method

All computational calculations were executed within the density functional theory (DFT) framework, employing the full-potential augmented plane waves plus local orbital (FP-LAPW+lo) method, as implemented through the WIEN2k code.[16] The exchange–correlation potential energies of the electrons were calculated in the generalized gradient approximation (GGA) *via* the Perdew–Burke–Ernzerhof (PBE) functional.[17]

The two-dimensional Nb_3C_2 MXene structure was constructed by selectively etching the A-group element from its corresponding MAX phase precursor to obtain a Nb_3C_2 monolayer. A vacuum layer of 15–20 Å was introduced along the *c*-direction to avoid the interactions between periodic layers. To evaluate the effect of substitutional Cr doping, one Nb atom in the supercell was substituted with a Cr atom. All structures were fully optimized prior to the electronic, magnetic and transport property calculations.[2,6]

Firstly, the unit cell and supercell structure of Nb_3C_2 and Cr-doped Nb_3C_2 were generated and optimized at 1000 ($19 \times 19 \times 2$) and 200 *k*-points within a $2 \times 12 \times 7$ *k*-mesh in the irreducible Brillouin zone (IBZ), respectively, using GGA-PBE. The expansion of valence wave functions within the Nb spheres was conducted up to $l_{max} = 10$. Additionally, the Fourier expansion of the charge density was pursued up to $G_{max} = 14$. For structural and electronic calculations, the potential was expanded within the Nb spheres, employing a combination of spherical harmonic functions and the Brillouin zone. The cut-off energy for the separation of valence and core electrons was chosen as −6 Ry, which corresponds to RMT $K_{max} = 7$, where RMT is the smallest of all atomic sphere radii and K_{max} determines the truncation of the reciprocal lattice expansion of the wave functions in the interstitial region.[18,19] Convergence of the total energy was set to 10^{-5} eV between successive iterations, with a Gaussian smearing factor of 0.05 eV. Atomic positions were fully relaxed until the maximum force on each atom was below 10^{-3} eV Å^{-1}. The plane-wave basis set was taken with an energy cut-off of 600 eV. For the electronic structure analysis, the Fermi level (E_F), defined as the highest occupied electronic state at 0 K, was set to 0 eV as the reference energy.[20,21]

Phonon dispersion calculations were performed using the PHONOPY package interfaced with WIEN2k to evaluate the dynamical stability of pristine and Cr-doped Nb_3C_2 structures. In addition, *ab initio* molecular dynamics (AIMD) simulations were carried out to examine thermal stability. The AIMD simulations were conducted in the canonical ensemble (NVT) using a Nosé–Hoover thermostat at 500 K. A time step of 1 fs was employed, and the total simulation time was 100 ps, corresponding to 10 000 MD steps.[22]

Spin-polarization calculations were carried out to determine the magnetic ordering of the 2D MXenes. Pristine Nb_3C_2 exhibited negligible magnetism (very small magnetic moments within numerical error), while Cr-doping stabilized a ferromagnetic state. The magnetic behavior was further evaluated using both GGA-PBE and GGA-PBE+*U*, where *U* represents the Hubbard potential. The *U* values of Nb (0.22 Ry = 3 eV)[20] and Cr (*U* = 0.15 Ry = 2 eV) were adopted from the literature, where similar parameters successfully captured the localized d-electron correlations.[23]

Although applying the *U* slightly increased the bandgap, the valence and conduction band levels near the Fermi level remained consistent, ensuring reliable results for electronic and optical properties.[24] The simplicity of this approach, along with the availability of all required inputs from first principles, makes it highly suitable for high-throughput computations, where it has gained wide acceptance.[25] The electronic transport

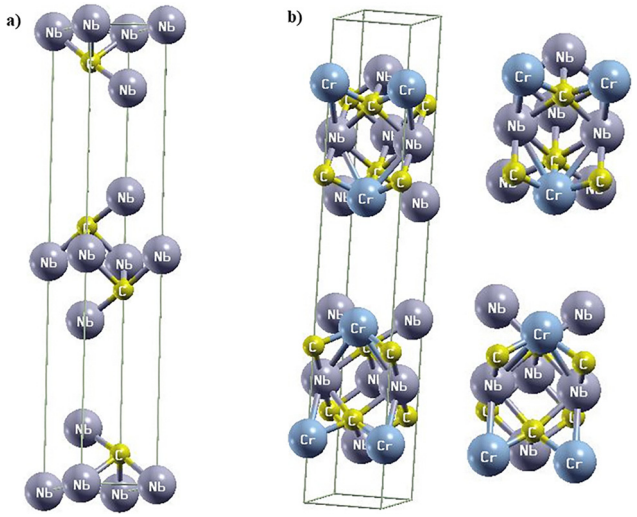

Fig. 1 (a) Crystal structure of pristine Nb_3C_2. (b) Schematic view of the 2 × 1 × 1 supercell of Cr-doped Nb_3C_2.

properties were calculated using the BoltzTraP2 code interfaced with WIEN2k under the constant relaxation time approximation (RTA), yielding the thermal and electrical conductivities.[26] To evaluate the Li storage capability of pristine and Cr-doped Nb_3C_2 for Li-ion batteries, we computed the adsorption energy,[27] the open circuit voltage (OCV),[28] and the theoretical capacity (Q).[29]

The adsorption energy (E_{ads}) was determined using:

$$E_{ads} = \frac{[E_{complex} - (E_{bare} + x\mu_M)]}{x} \quad (1)$$

The open-circuit voltage (OCV) was calculated using:

$$V = [E_{total}(Nb_3C_2) + xE_{total}(Li) - E_{total}(Li_xNb_3C_2)]/x \quad (2)$$

The theoretical capacity (Q) was determined from:

$$Q = \frac{nF}{M_f} \quad (3)$$

Here, $E_{total}(Nb_3C_2)$ and $E_{total}(Li_xNb_3C_2)$ denote the total energies per formula unit before and after Li intercalation, while $E_{total}(Li)$ is the energy per Li atom in bulk lithium; multiplying by x accounts for the total energy of x intercalated Li atoms during the process. In the theoretical capacity formula, 'n' is the number of electrons transferred per formula unit, F is the Faraday constant, and M_f is the mass of the formula unit.

3. Results and discussion

3.1. Structure prediction of novel MXenes

According to results obtained *via* first-principles DFT calculations, the newly designed Nb_3C_2 MXene structure was found to belong to the hexagonal geometry with the space group number 194 ($P6_3/mmc$) and lattice parameters $a = b = 3.131$ Å, $c = 19.24$ Å with $\alpha = \beta = 90^\circ$ and $\gamma = 120^\circ$. Two inequivalent niobium atoms were identified as Nb(1) and Nb(2), along with one carbon atom, having fractional coordinates Nb(1) (2/3, 1/3, 0.875), Nb(2) (0, 0, 0.5) and C: (1/3, 2/3, 0.924). The obtained lattice constant values are very close to the reported literature value of 3.3008 Å.[30]

To elucidate the effect of Cr doping in the Nb_3C_2 structure, a 2 × 1 × 1 supercell was generated. This supercell contains six Nb atoms and two C atoms. A 25% Cr-doped Nb_3C_2 structure was then optimized using 1000 k-points within a 2 × 12 × 7 k-mesh in the irreducible Brillouin zone (IBZ). The schematic views of pristine and Cr-doped Nb_3C_2 are shown in Fig. 1.

3.2. Structural and thermal stability

The phonon dispersion curves for both pristine and Cr-doped Nb_3C_2 are presented in Fig. 2. It is evident that no imaginary (negative) frequencies are present throughout the Brillouin zone, confirming the dynamical stability of both structures. A slight shift in phonon band separation is observed in the frequency range of approximately 10–15 THz between pristine and doped Nb_3C_2 (Fig. 2a and b), indicating modifications in interatomic interactions and bonding strength due to doping. Both systems exhibit three acoustic and several optical branches, as typically observed in two-dimensional materials.

The slope of the acoustic branches is slightly higher in pristine Nb_3C_2 as shown in Fig. 2a, compared to the doped structure in Fig. 2(b), suggesting a relatively higher phonon group velocity. Furthermore, the absence of a distinct gap between acoustic and

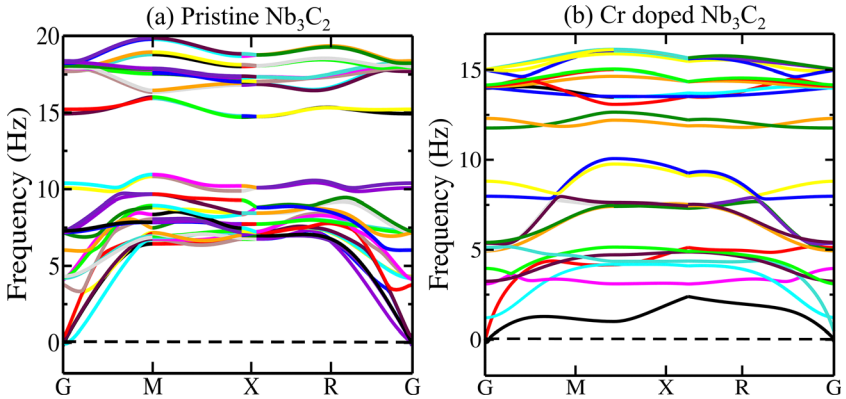

Fig. 2 Phonon dispersion curves of (a) pristine Nb_3C_2 and (b) Cr-doped Nb_3C_2 MXenes.

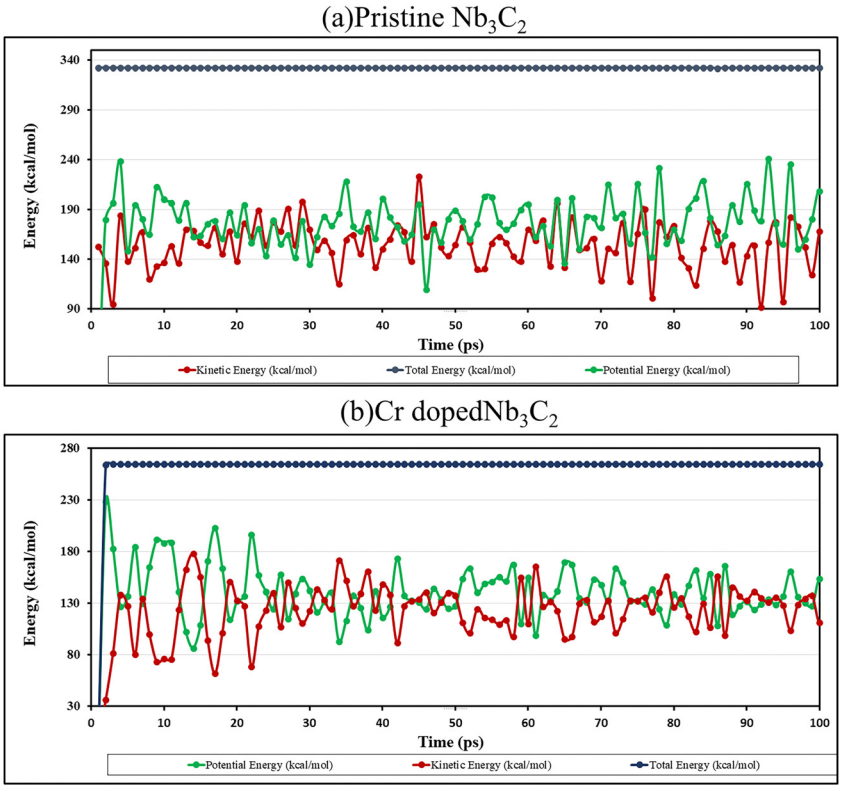

Fig. 3 AIMD simulation of (a) pristine Nb_3C_2 and (b) Cr-doped Nb_3C_2 at 500 K, showing energy evolution with atoms in their most stable position.

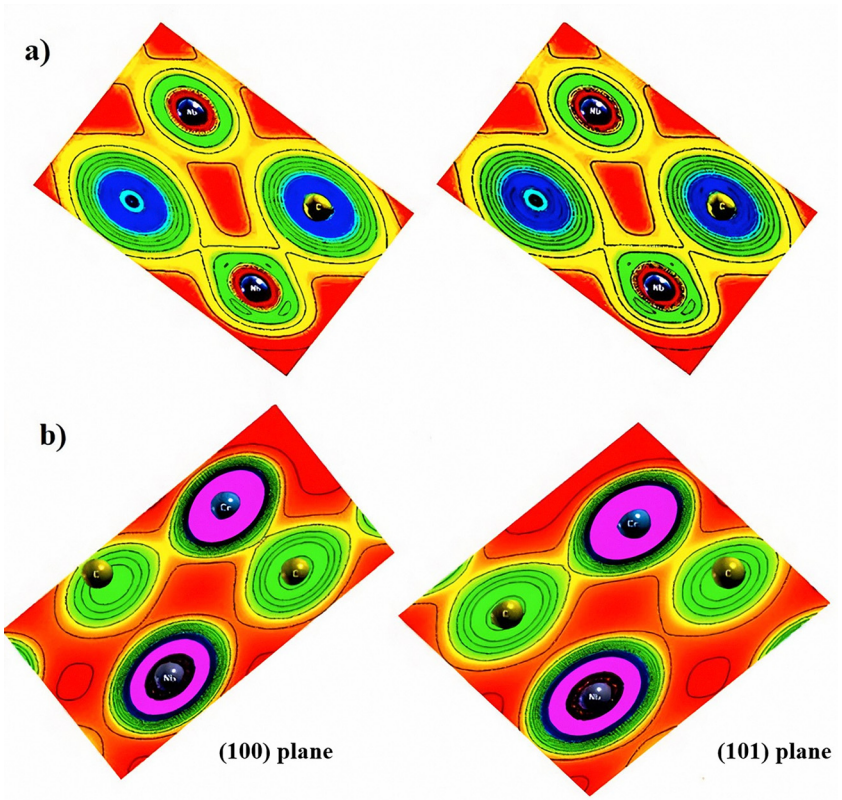

Fig. 4 Charge density distribution of (a) pristine Nb_3C_2 and (b) Cr doped Nb_3C_2 along the (100) plane and (110) crystallographic planes. The plots illustrate charge localization and bonding characteristics between Nb–C and Nb–Cr atoms, highlighting the electronic modification of electronic interactions upon Cr doping.

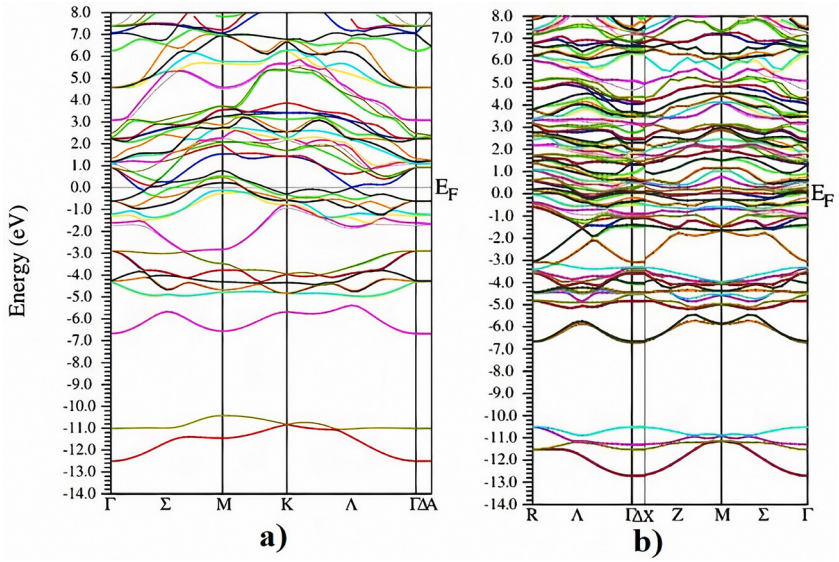

Fig. 5 Band structures of (a) pristine Nb_3C_2 calculated using sp-GGA and (b) Cr-doped Nb_3C_2.

optical modes may enhance acoustic–optical phonon scattering, which can influence the thermal conductivity of both pristine and doped Nb_3C_2 MXene layers.[31]

The energy evolution of pristine and Cr-doped Nb_3C_2 MXene systems during the AIMD simulations is presented in Fig. 3, with pristine Nb_3C_2 shown in Fig. 3a and Cr-doped Nb_3C_2 in Fig. 3b. The total energy of both structures remains nearly constant throughout the simulation, indicating good numerical stability. The potential, kinetic, and non-bonding energies exhibited moderate fluctuations around their average values, which are expected due to the thermal motion of atoms. For pristine Nb_3C_2 (Fig. 3a), energy variations remain confined within a narrow range over the 10 ps simulation, suggesting that the structural framework remains intact without significant distortion. A similar trend is observed for the Cr-doped Nb_3C_2 system (Fig. 3b), where the energy components fluctuate around equilibrium values without any noticeable drift in total energy. These stable energy oscillations confirm that Cr incorporation does not compromise the structural integrity of the MXene lattice, demonstrating that both systems maintain thermal stability under the simulated conditions.[22]

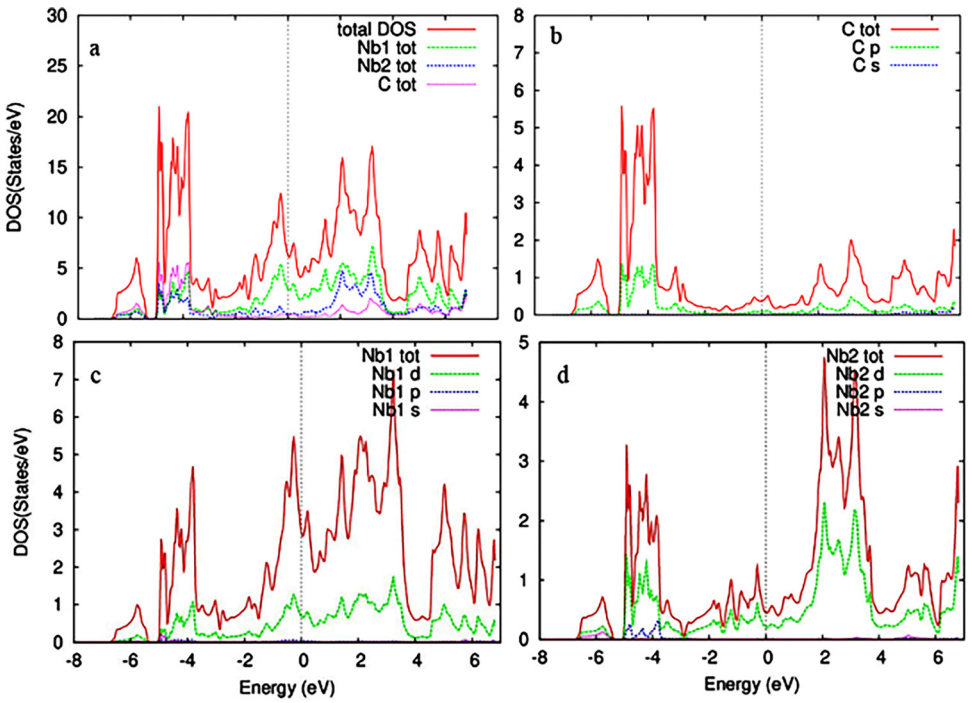

Fig. 6 (a) Total density of states (TDOS) of pristine Nb_3C_2 and (b)–(d) partial density of states (PDOS) of C, Nb_1, and Nb_2 atoms, respectively.

3.3. Electronic properties of pristine and Cr-doped Nb_3C_2

Exploring the electronic properties of a potential electrode requires determining whether the material exhibits metallic, semiconducting, or insulating behavior.[32] In this study, Cr atoms were employed as dopants to investigate the electronic characteristics, including charge density distribution, band structure, and density of states (DOS). The energy gaps between valence and conduction bands were identified from the calculated density of states (DOS) and band structure.[33]

Charge density plots provide direct insight into the bonding characteristics of the system.[34] Fig. 4(a) and (b) shows the electron density of pristine and Cr-doped Nb_3C_2 along the (100) and (110) planes. It is revealed that Cr-doping modifies the bonding nature between Nb and C atoms. As shown in

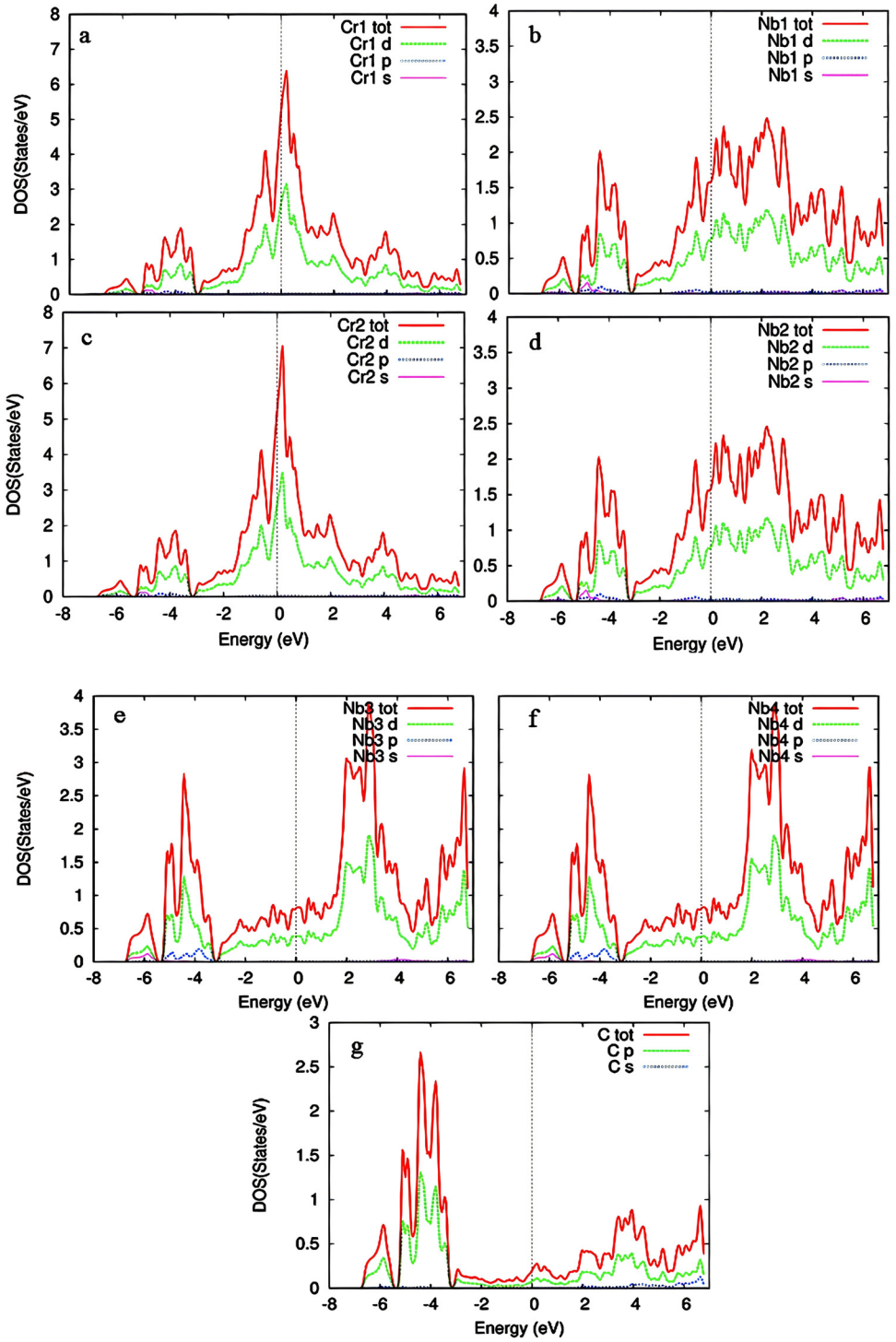

Fig. 7 Partial density of states (PDOS) of Cr-doped Nb_3C_2 in a 2 × 1 × 1 supercell: (a) Cr_1, (b) Nb_1, (c) Cr_2, (d) Nb_2, (e) Nb_3, (f) Nb_4, and (g) C atoms.

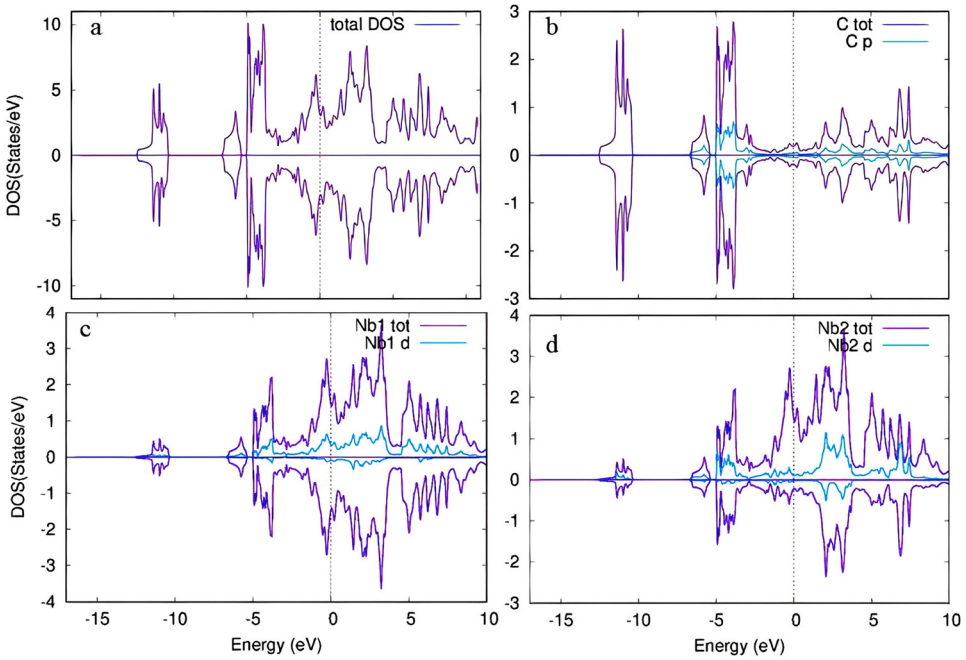

Fig. 8 Density of states (DOS) of pristine Nb_3C_2 calculated using spin-polarized GGA (sp-GGA): (a) total DOS (TDOS), (b) DOS and PDOS of C-2p states, (c) TDOS and PDOS of Nb_1-4d states, and (d) TDOS and PDOS of Nb_2-4d states.

Fig. 4(a), the charge density contour of pristine Nb_3C_2 indicates a covalent bond between C and Nb atoms, while in Fig. 4(b), Cr-doped Nb_3C_2 exhibits a covalent bond between Cr and C atoms due to the overlap of their valence electrons. In addition, the spherical charge distribution around Nb atoms in Nb_3C_2 indicates ionic bonding between the electronegative C atoms and electropositive Nb atoms. In the Cr-doped Nb_3C_2, the weak covalent interaction between Nb and C atoms suggests a weaker hybridization tendency of Nb towards C, as compared with pristine Nb_3C_2.[35] These features confirm that Cr doping significantly alters the bonding environment and electronic interactions in Nb_3C_2.

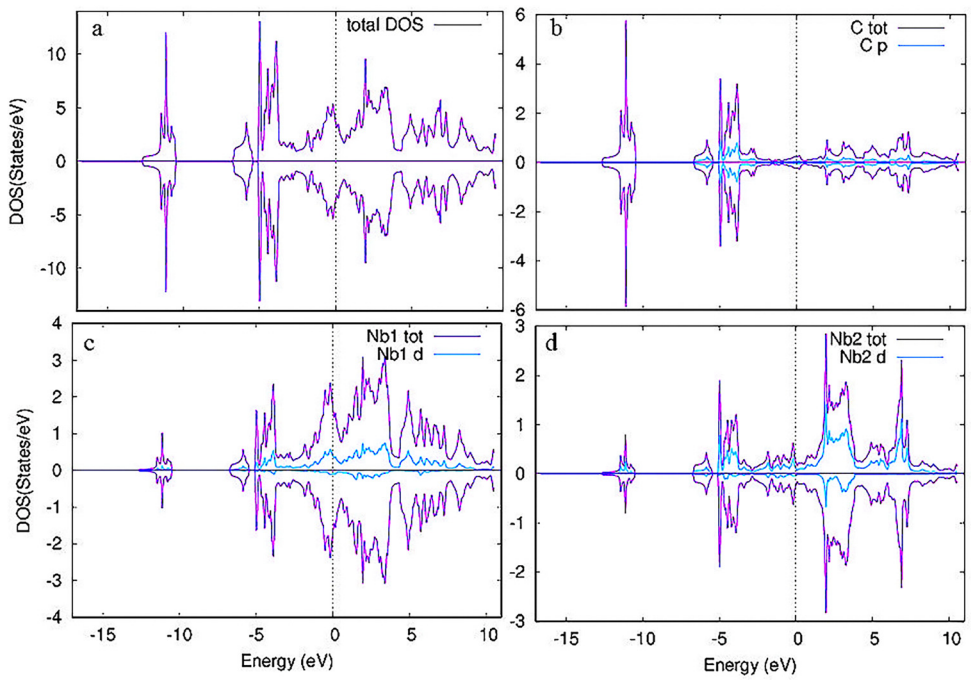

Fig. 9 Density of states (DOS) of pristine Nb_3C_2 calculated using spin-polarized GGA with Hubbard *U* correction (sp-GGA+*U*): (a) total DOS (TDOS), (b) TDOS and PDOS of C-2p states, (c) TDOS and PDOS of Nb_1-4d states, and (d) TDOS and PDOS of Nb_2-4d states.

Table 1 Magnetic moments of pristine Nb_3C_2 and Cr-doped Nb_3C_2

Compound	Atoms	Magnetic moment (PBE-GGA)	Magnetic moment (PBE-GGA+U)
Pristine Nb_3C_2	Nb_1 (μ_B)	0.00003	0.00026
	Nb_2 (μ_B)	−0.00002	−0.00007
	C (μ_B)	0.00001	−0.000001
	Interstitial (μ_B)	0.00013	0.00059
	Total (μ_B)	0.00024	0.00146
Cr-doped Nb_3C_2	Cr_1 (μ_B)	1.76157	2.51618
	Cr_2 (μ_B)	1.76010	2.55740
	Nb_1–Nb_4 (μ_B)	−0.03548	0.11141
		−0.03698	0.16468
		−0.02989	−0.07683
		−0.02989	−0.07441
	C (μ_B)	−0.04485	−0.07782
		−0.04473	−0.08433
		−0.01336	−0.02645
		−0.01323	−0.03146
	Interstitial (μ_B)	0.94320	2.08746
	Total (μ_B)	7.48972	12.04418

The interpretation of the band structure provides detailed insights into the electronic behaviour of materials, serving as a fundamental indicator of their conductivity and their responsiveness to doping-induced modifications. The band structure of pristine Nb_3C_2 (Fig. 5a) indicated metallic behavior, as the band gap was found to be zero.[36]

In contrast, Cr-doping (Fig. 3b) increased the density of electronic states around the Fermi level; however, the band gap for the Cr doped Nb_3C_2 structure also remained zero. This confirms that Nb_3C_2 retains its metallic character even after Cr doping. Moreover, Cr doping increases the electronic states above the Fermi level due to the additional energy levels introduced by Cr atoms within the crystal lattice, as evident from Fig. 5b.[37]

This expansion is shown to be due to the n-type doping effect of Cr atoms, bringing about distinct modifications in the pristine Nb_3C_2 band structure, which in turn influences the electrical conductivity of the material.[38] Band gap analysis therefore suggests that both pristine and doped Nb_3C_2 exhibit effective electrical conductivity, as this enables efficient electron transport during electrochemical processes.[39]

To estimate the number of states at different energy levels occupied by electrons, the partial and total density of states (PDOS and TDOS) for pristine and Cr-doped Nb_3C_2 were calculated, as shown in Fig. 6 and 7, respectively. For the TDOS, Fig. 6(a) shows a maximum peak in the density of states around −6.5 eV, indicating a high concentration of electrons at this energy level.[40]

For the PDOS of pristine Nb_3C_2 (Fig. 6a–d), the maximum electronic states at the Fermi level (E_F) mainly originate from the Nb_1-4d orbital states.[41] The valence band is dominated by C-2p states, with an admixture of Nb d-orbital contributions, confirming covalent Nb–C bonding.[42] Above the Fermi level, the conduction band is primarily composed of Nb_1-4d orbitals, with additional contributions from Nb_2-4d states, suggesting anisotropic electronic transport.[43] The dominance of Nb-4d orbitals near the Fermi level confirms its metallic conductivity, which is beneficial for electrochemical performance when used as an electrode material.[44]

Cr doping significantly increases the density of states per electron volt. At the Fermi level, the dominant contributions arise from Cr_1-3d and Cr_2-3d orbitals, with smaller contributions from Nb_1-4d and Nb_2-4d states. The upper part of the conduction band consists of states from Cr_1, Cr_2, Nb_1, Nb_2, Nb_3, and Nb_4 d orbitals. In the energy range of 2–4 eV above E_F, the conduction band is mainly dominated by Nb_3-4d and Nb_4-4d orbitals, with minor contributions from Cr_1-3d, Cr_2-3d, and Nb_1-4d and Nb_2-4d states. Meanwhile, C-2p orbitals contribute negligibly to the conduction band but play a major role in the valence band through hybridization with Nb_3-4d and Nb_4-4d orbitals.

As evident from Fig. 7, the density of states in both the valence and conduction bands cross the Fermi level without opening a gap, thereby confirming the metallic character of Cr-doped Nb_3C_2.[45] The PDOS plots show the orbital contributions of Cr, Nb, and C atoms in Cr-doped Nb_3C_2. Cr atoms (a) and (c) mainly contribute through d-states near the Fermi level, indicating strong hybridization. Nb atoms (b)–(f) also show dominant d-orbital contributions, crucial for electronic conductivity. C atoms (g) contribute primarily through p-states, supporting the overall electronic interaction in the heterostructure.

3.4. Magnetic properties

Magnetism in MXenes has not been extensively explored for the M_3C_2 phase, either theoretically or experimentally. For comparison, Ti_3C_2 magnetism has been briefly studied by Shien *et al.*, who reported ferromagnetic behavior.[46,47]

Herein, pristine Nb_3C_2 exhibited an essentially non-magnetic ground state, as the calculated magnetic moments for Nb_2 were $-0.00002\mu_B$ (GGA) and $-0.00007\mu_B$ (GGA+U), which were negligibly small and within the margin of computational error.[48] Although the PDOS of Nb_2 shows a slight asymmetry between spin-up and spin-down states (Fig. 8a), the imbalance is too weak to generate a measurable magnetic response in the whole compound. Consequently, the net magnetic moment is effectively zero, confirming the non-magnetic nature of pristine Nb_3C_2.

Fig. 8(b)–(d) further illustrates the DOS and PDOS of C-2p, Nb_1-4d, and Nb_2-4d states. By applying the Hubbard potential (GGA+U), the magnetic moment of the carbon atom became aligned with that of Nb_2 and anti-parallel to Nb_1, which enhanced the overall magnetic moment. This increase arises because the GGA+U correction shifts the partial density of states of Nb_1 and Nb_2, accounting for stronger electron–electron correlation effects[49] as shown in Fig. 9. Cr doping in Nb_3C_2 enhanced the magnetism and stabilized a ferromagnetic ground state.

Table 1 shows that pristine Nb_3C_2 is nearly non-magnetic with negligible total magnetic moment using both PBE-GGA and PBE-GGA+U calculations. Upon Cr doping, the system exhibits a substantial increase in magnetism (the total moment rising from $\sim$7.5 to $\sim$12.0μ_B), primarily originating from the strong spin polarization of Cr-3d states and significant interstitial contributions, while Nb and C atoms provide smaller site-dependent moments. Fig. 8 further supports this, as the

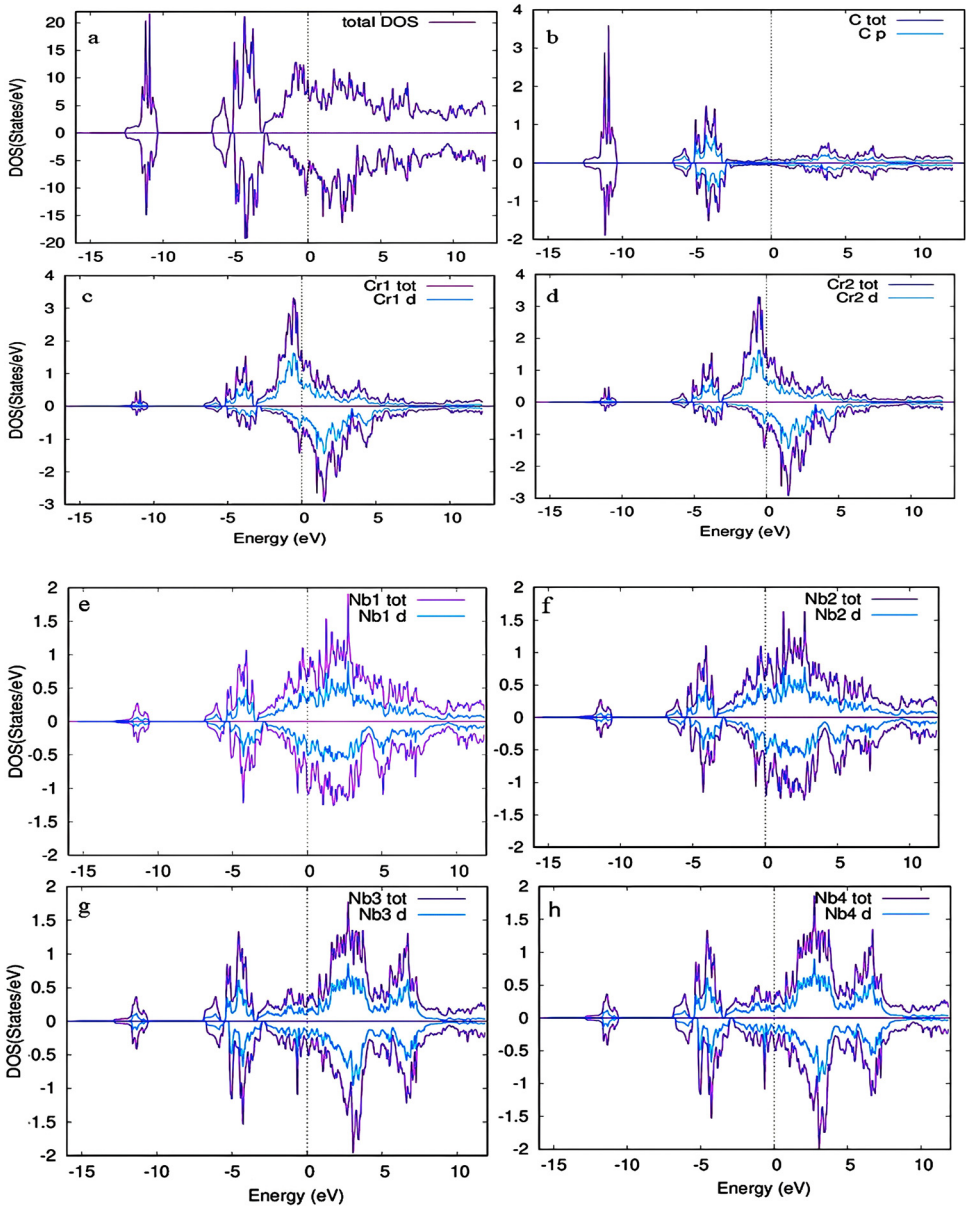

Fig. 10 Density of states (DOS) for Cr-doped Nb_3C_2 calculated using sp-GGA: (a) total DOS, (b) TDOS and PDOS of C-2p states, (c) and (d) TDOS and PDOS for Cr_1 and Cr_2 (total and 3d states, respectively), and (e)–(h) TDOS and PDOS for Nb_1, Nb_2, Nb_3 and Nb_4 (total and 3d states, respectively).

spin-polarized PDOS confirms the ferromagnetic nature through asymmetry of electronic states below and above the Fermi level for majority and minority spin channels.[50] The Cr-d orbitals (Fig. 10c and d) dominate the magnetism with strong spin polarization, whereas C-p orbitals (Fig. 10b) remain nearly symmetric. Nb-d states (Fig. 10e–h) display moderate asymmetry, indicating induced contributions through hybridization with Cr-d states. Overall, the net magnetic moment mainly arises from unpaired Cr-d electrons, with Nb atoms providing secondary polarization, thereby stabilizing robust ferromagnetism in Cr-doped Nb_3C_2, which is beneficial for charge storage and transport in lithium-ion batteries.

The calculated magnetic moment values for pristine Nb_3C_2 and Cr-doped Nb_3C_2 are summarized in Table 1.

3.5. Transport properties

The transport properties, including electrical conductivity, Seebeck coefficient, and thermal conductivity, were evaluated as a function of chemical potential at temperatures of 300 K, 500 K, and 700 K. These parameters provide insight into the charge-carrier behavior and electron transport efficiency in Nb_3C_2, which is essential for assessing its potential as an electrode material for energy storage applications.[51] Transport properties were also estimated for the lithiated systems of both pristine and Cr-doped Nb_3C_2, since lithiation and delithiation during Li-ion battery charge/discharge significantly influence charge-carrier mobility and the density of states near the Fermi level.[52]

The Seebeck coefficient is a key parameter for understanding charge-carrier behavior and transport efficiency.[53] Fig. 11 depicts

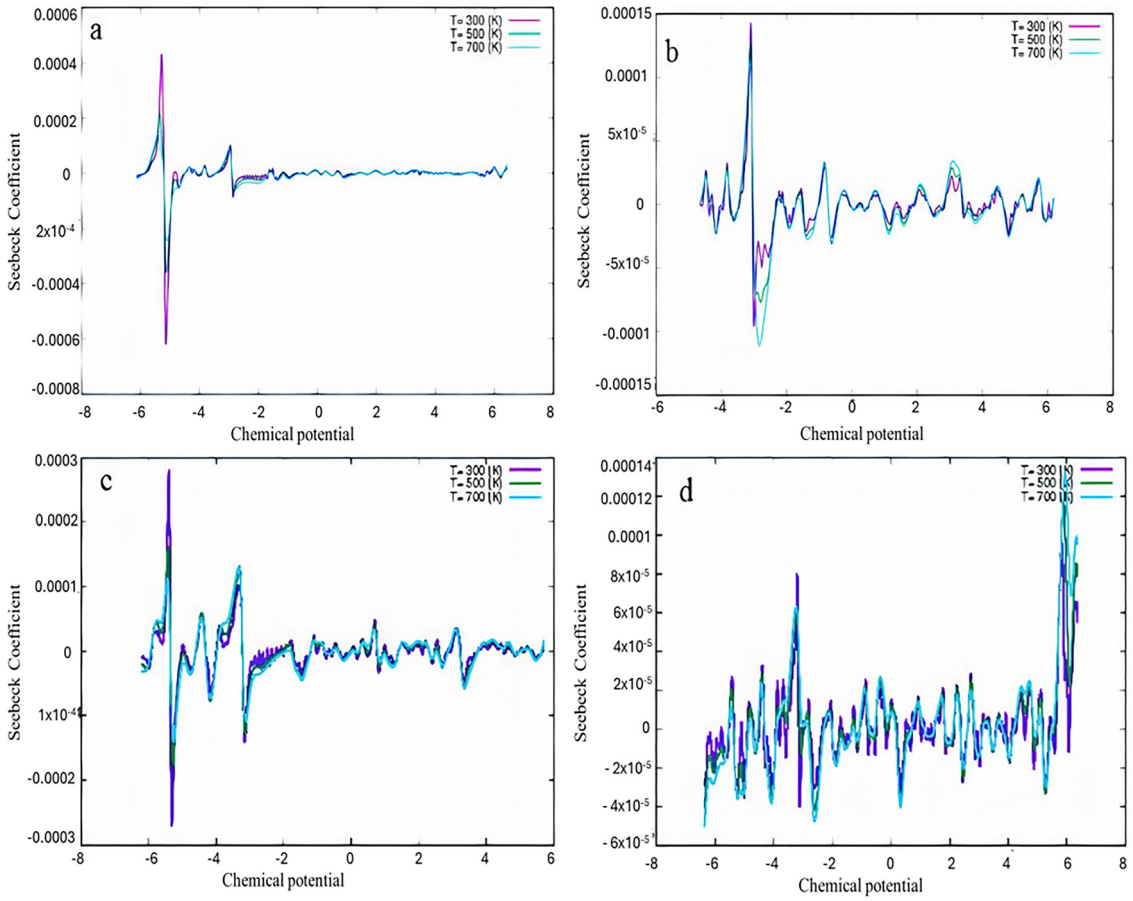

Fig. 11 Seebeck coefficient as a function of chemical potential at three different temperatures for the compounds: (a) pristine Nb_3C_2, (b) $Li_2Nb_3C_2$, (c) Cr-doped Nb_3C_2, and (d) Li_4–Cr-doped Nb_3C_2.

Table 2 Seebeck coefficient at different temperatures for lithiated and de-lithiated phases of pristine and Cr-doped Nb_3C_2

Temperature (K)	Nb_3C_2	$Li_2Nb_3C_2$	Cr-doped Nb_3C_2	$Li_4CrNb_3C_2$
300	4.2×10^{-4}	1.5×10^{-4}	2.9×10^{-4}	8.0×10^{-5}
500	2.0×10^{-4}	1.3×10^{-4}	1.8×10^{-4}	6.5×10^{-5}
700	1.0×10^{-4}	1.2×10^{-4}	1.2×10^{-4}	6.0×10^{-5}

the Seebeck coefficient as a function of chemical potential for various Nb_3C_2-based compounds. For pristine Nb_3C_2, Fig. 11(a) shows four distinct peaks at chemical potentials of −5.9 eV, −5.2 eV, −3.2 eV, and −3.0 eV. Outside this range, the Seebeck coefficient rapidly approaches zero, which indicates good transport performance. In contrast, lithiated Nb_3C_2, Cr-doped Nb_3C_2, and lithiated Cr-doped Nb_3C_2 (Fig. 11(b)–(d)) show smaller Seebeck values over the entire chemical potential range, consistent with strong metallic behavior. In Li-ion battery electrodes, metallic conductivity is essential for efficient charge transport.[54] These results suggest that the lithiated phases, particularly $Li_2Nb_3C_2$ and Li_4Cr-doped Nb_3C_2, exhibit high metallic conductivity and may provide more efficient electronic transport during Li-ion battery operation compared to pristine Nb_3C_2.

The maximum values of the Seebeck coefficient for the different compounds at various temperatures are summarized in Table 2. The results show that, with increasing temperature, the carrier concentration increases, leading to a reduction in the Seebeck coefficient, as expected for metallic systems. This behavior is consistent with the metallic nature of all compounds.

Electrical conductivity reflects the ease of electron flow in a material, and materials with efficient transport typically exhibit high conductivity. In metallic systems, conductivity generally decreases with increasing temperature but increases with chemical potential, due to higher carrier concentration and improved mobility.[55] As shown in Fig. 12a and c, the electrical conductivity approaches zero near −5.5 eV at 300 K for both delithiated Nb_3C_2 and delithiated Cr-doped Nb_3C_2. In contrast, the lithiated phases shown in Fig. 12(b) and (d) exhibited significantly higher conductivity than their delithiated counterparts, indicating enhanced electron conduction during Li-ion battery operation. The maximum values of electrical conductivity are summarized in Table 3.

Fig. 13 depicts the thermal conductivity of Nb_3C_2-based systems as a function of chemical potential at three different temperatures. For all compounds, κ increases with temperature, consistent with their metallic nature.[56] Pristine Nb_3C_2 shows a smoother variation in thermal conductivity with chemical

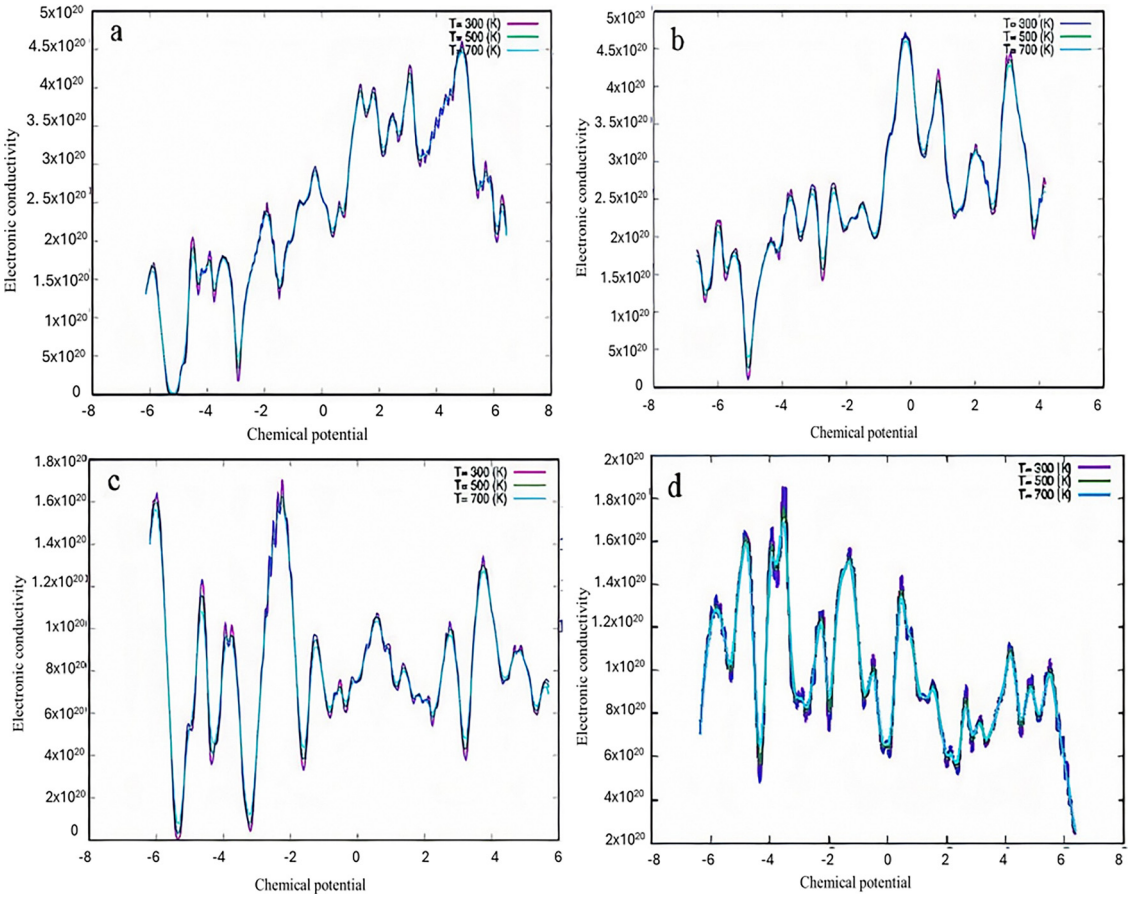

Fig. 12 Electronic conductivity as a function of chemical potential at three different temperatures for: (a) pristine Nb_3C_2, (b) $Li_2Nb_3C_2$, (c) Cr-doped Nb_3C_2, and (d) Li_4–Cr-doped Nb_3C_2.

Table 3 Electronic conductivity of lithiated and delithiated phases of pristine and Cr-doped Nb_3C_2 at room temperature

Compound	Electrical conductivity (S m^{-1})
$Li_2Nb_3C_2$	4.7×10^{20}
Nb_3C_2	4.4×10^{20}
LiCr–Nb_3C_2	1.9×10^{20}
Cr–Nb_3C_2	1.7×10^{20}

potential, whereas the other systems exhibit stronger variations, maintaining higher conductivity over a broader chemical potential (μ) range. Combined with the Seebeck coefficient and electrical conductivity results, these trends indicate that lithiation significantly enhances both charge and heat transport.[57] In particular, $Li_2Nb_3C_2$ and Li_4–Cr-doped Nb_3C_2 demonstrate excellent transport properties, making them promising candidates for efficient Li-ion battery electrodes.

3.6. Electrochemical performance of MXenes as electrode materials

Metallic behavior is a desirable characteristic for electrode materials.[58] The electronic properties confirm that both pristine Nb_3C_2 and Cr-doped Nb_3C_2 are metallic, thereby fulfilling this requirement. In electrochemical applications, intercalating species play a crucial role, with Li^+ ions being the most widely used in Li-ion batteries.[59] In this study, Li^+ intercalation into pristine Nb_3C_2 and Cr-doped Nb_3C_2 MXenes was investigated to evaluate their storage capability as electrode materials. The electrochemical suitability of these MXenes was examined through adsorption energy analysis.

3.6.1. Adsorption energy. Eqn (1) was employed to calculate the adsorption energies of lithium ions adsorbed on pristine and Cr-doped Nb_3C_2. The adsorption energy was further used to estimate the average intercalation potential of the materials.[60] In this study, the calculated adsorption energies of a Li atom on pristine Nb_3C_2 and Cr-doped Nb_3C_2 were -1.20 eV and -1.48 eV, respectively. A negative value of E_{ad} indicates that the corresponding atom favors adsorption on the surface rather than forming clusters.[61,62] Cr-doped Nb_3C_2 exhibits a more negative adsorption energy, indicating that Li adsorption is energetically more favorable compared to that on pristine Nb_3C_2. Similar trends have been reported in other doped MXenes; for instance, V-doped Ti_2Co_2 shows more negative energies in the range of -1.9 eV to -2.8 eV compared to its undoped system.[63] This behavior is attributed to the additional electronic states introduced by the dopant atoms, which enhance charge transfer and orbital hybridization with

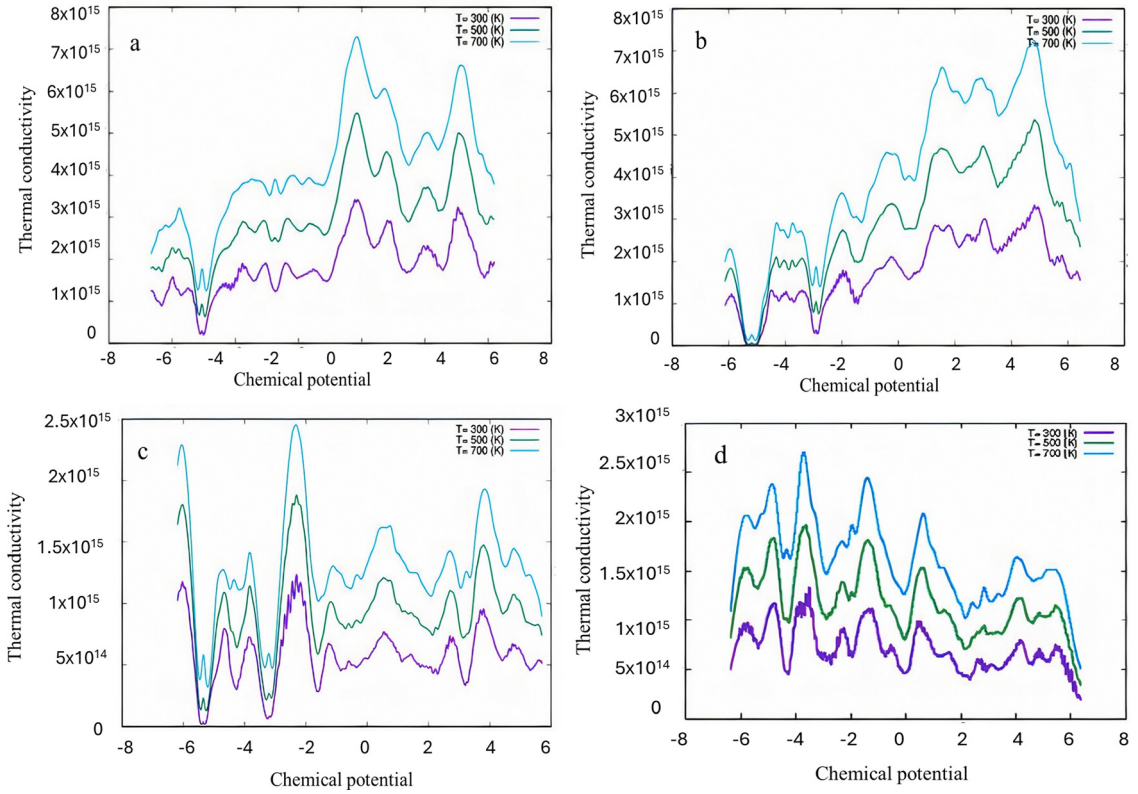

Fig. 13 Thermal conductivity as a function of chemical potential at three different temperatures for the compounds: (a) pristine Nb_3C_2, (b) $Li_2Nb_3C_2$, (c) Cr-doped Nb_3C_2, and (d) Li_4–Cr-doped Nb_3C_2.

Li, thereby strengthening the binding interaction.[64] In the present case, the introduction of Cr atoms modifies the electronic density of states near the adsorption site, increasing the interaction with Li atoms and thereby improving adsorption favorability. According to our calculations, a unit cell and a 2 × 1 × 1 supercell can accommodate only 2 and 4 Li atoms per formula unit, respectively. Beyond the adsorption of two Li ions per formula unit, the system reaches a saturation point. The saturation point in a structure varies depending on coulombic repulsion, structural distortion, and the lack of favorable adsorption sites.[65]

3.6.2. Open circuit voltage (OCV). The open-circuit voltage (OCV) is an important parameter for evaluating the electrochemical performance of electrode materials in lithium-ion batteries. It provides insights into the average lithiation potential of the material, which directly influences both energy density and cycling stability.[66] In this work, the OCV was determined using eqn (2) for pristine and Cr-doped Nb_3C_2 systems with the adsorption of 2 and 4 Li atoms per formula unit, respectively.

$$V = [E_{total}(Nb_3C_2) + xE_{total}(Li) - E_{total}(Li_2Nb_3C_2)]/x \quad (4)$$

$$V = [E_{total}(CrNb_3C_2) + xE_{total}(Li) - E_{total}(Li_4CrNb_3C_2)]/x \quad (5)$$

Here, $E_{total}(Nb_3C_2)$ and $E_{total}(Li_2Nb_3C_2)$ represent the total energies per formula unit of pristine Nb_3C_2 without and with Li intercalation, respectively. Similarly, $E_{total}(Li_4CrNb_3C_2)$ and $E_{total}(CrNb_3C_2)$ correspond to the total energies of the Cr doped system before and after Li intercalation, respectively. $E_{total}(Li)$ denotes the total energy of an isolated Li atom.[67]

The corresponding intercalation reactions can be expressed as:

$$Nb_3C_2 + 2Li \rightarrow Li_2Nb_3C_2 \quad (6)$$

$$CrNb_3C_2 + 4Li \rightarrow Li_4CrNb_3C_2 \quad (7)$$

The calculated OCV values for Li^+ extraction are 1.20 V for $Li_2Nb_3C_2$ and 1.48 V for $Li_4CrNb_3C_2$. The positive voltages indicate energetically favorable Li intercalation. Notably, Cr-doped Nb_3C_2 exhibits a higher OCV compared to the pristine system. This enhancement can be attributed to the additional electronic states introduced by Cr atoms, which strengthen the interaction with Li and stabilize the intercalated structure. These values are consistent with previously reported OCV values for other MXene materials; for example, Ti_2C exhibits an OCV of approximately 1.22 V.[68]

3.6.3. Theoretical capacity. The theoretical capacity is a key property of energy storage materials. Here, the theoretical capacity (Q) was estimated using eqn (3) for both pristine and Cr-doped Nb_3C_2 systems.

The theoretical capacity of pristine Nb_3C_2 for Li-ion batteries was found to be 169 mAh g^{-1}, which is comparable to the reported value of Nb_2C (170 mAh g^{-1}).[69] In contrast, Cr-doped Nb_3C_2 exhibits a significantly higher storage capacity of

280 mAh g^{-1}, indicating that Cr doping substantially enhances the Li-ion storage performance of the MXene.

4. Conclusions

Using first-principles calculations, we systematically investigated the structural, electronic, magnetic, and transport properties of pristine Nb_3C_2 and Cr-doped Nb_3C_2, as well as their potential as electrode materials for Li-ion batteries. Structural analysis confirmed that Nb_3C_2 and Cr-doped Nb_3C_2 adopt hexagonal ($P6_3/mmc$) and orthorhombic ($Pmm2$) crystal structures, respectively. Phonon and AIMD results confirm that both pristine Nb_3C_2 and Cr-doped Nb_3C_2 are dynamically and thermally stable, with no significant structural distortions observed. These findings validate the reliability of the subsequent electronic and magnetic property calculations.

Charge density contours revealed that Cr doping substantially modifies the Nb–C bonding nature, while the band structures and density of states (DOS) confirm metallic behavior (indirect zero-band gap) in both systems, primarily originating from Nb 4d states. Moreover, substitutional Cr doping transforms non-magnetic pristine Nb_3C_2 into a ferromagnetic material with a finite magnetic moment, making it a promising candidate for 2D spintronic applications.

Transport property evaluations based on Boltzmann transport theory demonstrate that lithiation significantly enhances charge and heat transport. In particular, $Li_2Nb_3C_2$ and Li_4Cr-doped Nb_3C_2 exhibit high electrical and thermal conductivities with low Seebeck coefficients, confirming their metallic character and suitability as Li-ion battery electrodes. Furthermore, Cr-doped Nb_3C_2 outperforms pristine Nb_3C_2, suggesting superior transport performance for high-efficiency energy storage applications.

Electrochemical analysis further supports Cr-doped Nb_3C_2 as a promising electrode material, owing to its higher electronic conductivity, higher open-circuit voltage, and improved theoretical capacity compared to pristine Nb_3C_2. These improved electrochemical and transport properties make Cr-doped Nb_3C_2 a potential candidate for high performance lithium-ion battery electrodes, particularly in applications requiring fast charge transport and high energy density, such as portable electronic devices and electric vehicles. Overall, these findings demonstrate that Cr doping is an effective strategy for tailoring the properties of Nb_3C_2 MXenes, underscoring their strong potential for next-generation spintronic and energy storage applications.

Conflicts of interest

The authors declare that the research was conducted in the absence of any commercial or financial relationships that could be construed as a potential conflict of interest.

Data availability

The computational data that support the findings of this study are available upon request. All the related data are presented in the form of figures and tables in the manuscript.

Acknowledgements

The authors gratefully acknowledge the School of Interdisciplinary Engineering & Science (SINES) Islamabad, National University of Science and Technology, for providing computational resources and facilities to support this work.

References

1 B. Zhang, Y. Huang, W. Bao, B. Wang, Q. Meng, L. Fan and Q. Zhang, Two-Dimensional Stable Transition Metal Carbides MnC and NbC with Prediction and Novel Functionalizations, *RSC Adv.*, 2018, **8**, 12345–12356, DOI: 10.1039/C8RA12345A.

2 X. Zhang, Z. Zhang and Z. Zhou, MXene-based materials for electrochemical energy storage, *J. Energy Chem.*, 2018, **27**, 73–85, DOI: 10.1016/j.jechem.2017.08.004.

3 Y. I. Jhon, I. K. Han, J. H. Lee and Y. M. Jhon, Microscopic understanding of exceptional orientation-dependent tensile and fracture responses of two-dimensional transition-metal carbides, *Appl. Surf. Sci.*, 2022, **585**, 152557, DOI: 10.1016/j.apsusc.2021.152557.

4 J. Pang, R. G. Mendes, A. Bachmatiuk, L. Zhao, H. Q. Ta, T. Gemming, H. Liu, Z. Liu and M. H. Rümmeli, Applications of 2D MXenes in energy conversion and storage systems, *Chem. Soc. Rev.*, 2019, **48**, 72–133, DOI: 10.1039/C8CS00324F.

5 A. Zaheer, S. A. Zahra, M. Z. Iqbal, A. Mahmood, S. A. Khan and S. Rizwa, Nickel-adsorbed two-dimensional Nb_2C MXene for enhanced energy storage applications, *RSC Adv.*, 2022, **12**, 4624–4633, DOI: 10.1039/D2RA00014H.

6 M. Ghidiu, M. Naguib, C. Shi, O. Mashtalir, L. M. Pan, B. Zhang, J. Yang, Y. Gogotsi, S. J. L. Billinge and M. W. Barsoum, Synthesis and characterization of two-dimensional Nb_4C_3 (MXene), *Chem. Commun.*, 2014, **50**, 9517–9520, DOI: 10.1039/C4CC03366C.

7 B. Shen, X. Liao, X. Zhang, H.-T. Ren, J.-H. Lin, C.-W. Lou and T.-T. Li, Synthesis of Nb_2C MXene-based 2D layered structure electrode material for high-performance battery-type supercapacitors, *Phys. Chem. Chem. Phys.*, 2020, **22**, 23900–23908, DOI: 10.1039/D0CP03726A.

8 N. Sultana, A. A. Amin, E. J. Payton and W. K. Kim, Insights into Nb_2C and Nb_2CO_2 as high-performance anodes for sodium- and lithium-ion batteries: An *ab initio* investigation, *arXiv*, 2025, preprint, arXiv:2504.08953, DOI: 10.48550/arXiv.2504.08953.

9 U. Kalsoom, S. Khan, M. Kashif, H. S. Yaseen, S. A. Hussain, S. Azizi and M. Maaza, MXene-based hybrid composites for lithium-ion batteries: advances in synthesis strategies and electrochemical performance, *Ionics*, 2025, 1–21.

10 R. Akhter and S. S. Maktedar, MXenes: a comprehensive review of synthesis, properties, and progress in supercapacitor applications, *J. Materiomics*, 2023, **9**(6), 1196–1241, DOI: 10.1016/j.jmat.2023.08.011.

11 J. Jiang, Y. Zou, A. Arramel, F. Li, J. Wang, J. Zou and N. Li, Intercalation engineering of MXenes towards highly

efficient photo(electrocatalytic) hydrogen evolution reactions, *J. Mater. Chem. A*, 2021, **9**, 24195–24214, DOI: 10.1039/D1TA07332J.

12 Z. Wang, Z. Dong, B. Wu, Z. Wang, Z. Qiu, D. Wang, Q. Zeng, X. Liu, K. N. Hui, Z. Liu and Y. Zhang, Unlocking the critical roles of N, P co-doping in MXene for lithium–oxygen batteries: elevated d-band center and expanded interlayer spacing, *J. Colloid Interface Sci.*, 2024, **676**, 368–377, DOI: 10.1016/j.jcis.2024.07.138.

13 K. Arole, S. E. Pas, R. M. Thakur, L. A. Amiouny, M. H. Kabir, M. Dujovic, M. Radovic, J. L. Lutkenhaus, M. J. Green and H. Liang, Effects of intercalation on ML-Ti_3C_2Tz MXene properties and friction performance, *ACS Appl. Mater. Interfaces*, 2024, **16**(46), 60538–60548, DOI: 10.1021/acsami.4c12157.

14 H. Qian, H. Ren, Y. Zhang, X. He, W. Li, J. Wang, J. Hu, H. Yang, H. M. K. Sari, Y. Chen and X. Li, Surface doping vs. bulk doping of cathode materials for lithium-ion batteries: a review, *Electrochem. Energy Rev.*, 2022, **5**(4), 2.

15 R. D. Shannon, Revised effective ionic radii and systematic studies of interatomic distances in halides and chalcogenides, *Acta Crystallogr., Sect. A: Cryst. Phys., Diffr., Theor. Gen. Crystallogr.*, 1976, **32**, 751–767, DOI: 10.1107/S0567739476001551.

16 G. R. Berdiyorov, Optical properties of functionalized $Ti_3C_2T_2$ (T = F, O, OH) MXene: first-principles calculations, *AIP Adv.*, 2016, **6**(5), 055105, DOI: 10.1063/1.4943752.

17 P. Blaha, K. Schwarz, G. K. H. Madsen, D. Kvasnicka and J. Luitz, *WIEN2k, An Augmented Plane Wave + Local Orbitals Program for Calculating Crystal Properties*, Technical University of Vienna, Austria, 2001, pp. 1–302.

18 T. W. Keal and D. J. Tozer, A semiempirical generalized gradient approximation exchange–correlation functional, *J. Chem. Phys.*, 2004, **121**(12), 5654–5660, DOI: 10.1063/1.1778374.

19 W. Chen, J. H. Pöhls, G. Hautier, D. Broberg, S. Bajaj, U. Aydemir, Z. M. Gibbs, H. Zhu, M. Asta, G. J. Snyder and B. Meredig, Understanding thermoelectric properties from high-throughput calculations: trends, insights, and comparisons with experiment, *J. Mater. Chem. C*, 2016, **4**(20), 4414–4426, DOI: 10.1039/C5TC04339E.

20 J. Carrete; N. Mingo; S. Wang and S. Curtarolo Nanograined half-Heusler semiconductors as advanced thermoelectrics: an *ab initio* high-throughput statistical study, *arXiv*, 2014, preprint, arXiv:1408.5859, DOI: 10.48550/arXiv.1408.5859.

21 M. Miyata, T. Ozaki, T. Takeuchi, S. Nishino, M. Inukai and M. Koyano, High-throughput screening of sulfide thermoelectric materials using electron transport calculations with OpenMX and BoltzTraP, *J. Electron. Mater.*, 2018, **47**, 3254–3259, DOI: 10.1007/s11664-017-6020-9.

22 A. Shamsieva, A. Evseev, S. Kaviani, O. V. Nedopekin, H. Zakaryan and I. Piyanzina, DFT analysis of furan-based covalent organic framework as electrode materials for lithium and calcium ion batteries, *Comput. Theor. Chem.*, 2025, **125**, 115445, DOI: 10.1016/j.comptc.2025.115445.

23 J. Fatheema, M. Fatima, N. B. Monir, S. A. Khan and S. Rizwan, A comprehensive computational and experimental analysis of stable ferromagnetism in layered 2D Nb-doped Ti_3C_2 MXene, *Phys. E*, 2020, **124**, 114253, DOI: 10.1016/j.physe.2020.114253.

24 Z. Tong, Y. Suo, S. Zhang and J. Yang, Spin-polarized DFT+U study of surface-functionalized Cr_3C_2 MXenes: tunable electronic and magnetic behavior for spintronics, *Materials*, 2025, **18**(15), 3709, DOI: 10.3390/ma18153709.

25 F. Aguilera-Granja, R. H. Aguilera-del-Toro and J. L. Morán-López, A first-principles systematic study of the structural, electronic, and magnetic properties of Heusler X_2MnZ with X = Fe, Co, Ni, Cu, Ru, Rh, Pd, Ag, Pt, Au and Z = Al, Si, Ga, Ge, In and Sn, *Mater. Res. Express*, 2019, **6**(10), 106118, DOI: 10.1088/2053-1591/ab243c.

26 L. Bassman Oftelie, P. Rajak and R. K. Kalia, *et al.*, Author Correction: Active learning for accelerated design of layered materials, *npj Comput. Mater.*, 2022, **8**, 215, DOI: 10.1038/s41524-022-00902-8.

27 F. Ricci, W. Chen, U. Aydemir, G. J. Snyder, G. M. Rignanese, A. Jain and G. Hautier, An *ab initio* electronic transport database for inorganic materials, *Sci. Data*, 2017, **4**, 170085, DOI: 10.1038/sdata.2017.85.

28 L. Wang, W. Liu, F. Bai, X. Zheng, C. Yin, J. Wei, J. Ma, H. Bai and B. Dong, Theoretical study on lithium storage performance of V-doped Ti_2CO_2 MXene, *RSC Adv.*, 2024, **14**, 19945, DOI: 10.1039/d4ra03618b.

29 J. W. Gonzalez; S. Vizcaya and E. Suarez Morell V2C-based lithium batteries: the influence of magnetic phase and Hubbard interaction, *arXiv*, 2022, preprint, arXiv:2204.04764, DOI: 10.48550/arXiv.2204.04764.

30 R.-W. Yan, X.-H. Li, R.-Z. Zhang and H.-L. Cui, Computational investigation on Cr-doped Sc_2CO_2 MXene under strain for electronic properties, quantum capacitance, and photocatalytic activity, *Langmuir*, 2024, **40**(37), 19619–19630, DOI: 10.1021/acs.langmuir.4c02282.

31 X. Yan, W. Cao and H. Li, Thermoelectric properties of $X_3N_2O_2$ (X = Hf, Zr) MXene monolayers: a first-principles study, *RSC Adv.*, 2023, **13**, 18323–18327, DOI: 10.1039/D3RA02835F.

32 F. B. Oliveira, E. N. Lima, M. C. da Silva, A. L. da Rosa and T. Frauenheim, Exploring charge density distribution and electronic properties of hybrid organic-germanium layers, *Phys. Chem. Chem. Phys.*, 2020, **22**, 22055–22065, DOI: 10.1039/D0CP03024D.

33 M. Fatima, J. Fatheema, N. B. Monir, A. H. Siddique, B. Khan, A. Islam, D. Akinwande and S. Rizwan, Nb-doped MXene with enhanced energy storage capacity and stability, *Front. Chem.*, 2020, **8**, 168, DOI: 10.3389/fchem.2020.00168.

34 Q. Sun, Z. Fu and Z. Yang, Tunable magnetic and electronic properties of the Cr-based MXene (Cr_2C) with functional groups and doping, *J. Magn. Magn. Mater.*, 2020, **514**, 167141, DOI: 10.1016/j.jmmm.2020.167141.

35 M. Khazaei, M. Arai, T. Sasaki, C.-Y. Chung, N. S. Venkataramanan, M. Estili, Y. Sakka and Y. Kawazoe, Novel electronic and magnetic properties of two-dimensional transition metal carbides and nitrides, *Adv. Funct. Mater.*, 2013, **23**, 2185–2192, DOI: 10.1002/adfm.201202502.

36 B. Soundiraraju and B. K. George, Two-dimensional titanium nitride (Ti_2N) MXene: synthesis, characterization, and potential application as surface-enhanced Raman scattering substrate, *ACS Nano*, 2017, **11**, 8892–8900, DOI: 10.1021/acsnano.7b03129.

37 B. Anasori, M. R. Lukatskaya and Y. Gogotsi, 2D metal carbides and nitrides (MXenes) for energy storage, *Nat. Rev. Mater.*, 2017, **2**, 16098, DOI: 10.1038/natrevmats.2016.98.

38 F. Ebisawa, T. Kurokawa and S. Nara, Electrical properties of polyacetylene/polysiloxane interface, *J. Appl. Phys.*, 1983, **54**, 3255–3259, DOI: 10.1063/1.332488.

39 I. R. Shein and A. L. Ivanovskii, Planar nano-block structures $Ti_{n+1}Al_{0.5}C_n$ and $Ti_{n+1}C_n$ (n = 1, 2) from MAX phases: structural, electronic properties and relative stability from first-principles calculations, *Superlattices Microstruct.*, 2012, **52**(2), 147–157, DOI: 10.1016/j.spmi.2012.04.014.

40 A. N. Yaresko, Electronic band structure and exchange interactions in ferromagnetic CrO_2, *Phys. Rev. B: Condens. Matter Mater. Phys.*, 2008, **77**, 115106, DOI: 10.1103/PhysRevB.77.115106.

41 S. L. Dudarev, G. A. Botton, S. Y. Savrasov, C. J. Humphreys and A. P. Sutton, Electron-energy-loss spectra and the structural stability of nickel oxide: an LSDA + U study, *Phys. Rev. B:Condens. Matter Mater. Phys.*, 1998, **57**, 1505–1509, DOI: 10.1103/PhysRevB.57.1505.

42 Y. Chen, X. Li, Z. Wang, J. Zhou and Z. Sun, Magnetic properties and tunable electronic structures of transition-metal-doped MXenes: a first-principles study, *J. Phys. Chem. C*, 2019, **123**, 17987–17994, DOI: 10.1021/acs.jpcc.9b03654.

43 H. Wang, H. Feng and J. Li, *et al.*, Graphene and graphene-like anode materials for lithium-ion batteries, *Adv. Mater.*, 2014, **26**, 4880–4900, DOI: 10.1002/adma.201306031.

44 G. J. Snyder and E. S. Toberer, Complex thermoelectric materials, *Nat. Mater.*, 2008, **7**, 105–114, DOI: 10.1038/nmat2090.

45 B. Xu, Y. Qi and C. Liu, *et al.*, Recent progress in MXene-based materials for electrochemical energy storage, *Adv. Funct. Mater.*, 2020, **30**, 1905812, DOI: 10.1002/adfm.201905812.

46 D. Beretta, N. Neophytou, J. M. Hodges, M. G. Kanatzidis, D. Narducci, M. Martin-Gonzalez, M. Beekman, B. Balke, G. Cerretti, W. Tremel, A. Zevalkink, A. I. Hofmann, C. Müller, B. Dörling, M. Campoy-Quiles and M. Caironi, Thermoelectrics: from history, a window to the future, *Mater. Sci. Eng., R*, 2019, **138**, 100501, DOI: 10.1016/j.mser.2018.09.001.

47 G. Berdiyorov, Effect of lithium and sodium ion adsorption on the electronic transport properties of Ti_3C_2 MXene, *Appl. Surf. Sci.*, 2015, **359**, 161–165, DOI: 10.1016/j.apsusc.2015.10.050.

48 J.-M. Tarascon and M. Armand, Issues and challenges facing rechargeable lithium batteries, *Nature*, 2001, **414**, 359–367, DOI: 10.1038/35104644.

49 B. Hammer and J. K. Nørskov, Theoretical surface science and catalysis—calculations and concepts, *Adv. Catal.*, 2000, **45**, 71–129, DOI: 10.1016/S0360-0564(02)45013-4.

50 M. Xia, T. Zhang, J. Wu, W. Lu, Z. Pan and J. Qiao, Transition metal layer substitution in Mo_2CS_2 MXene: enhanced Li adsorption and electronic structure modulation, *ACS Omega*, 2023, **8**, 23412–23420, DOI: 10.1021/acsomega.3c02080.

51 Q. Tang, Z. Zhou and P. Shen, Are MXenes promising anode materials for Li ion batteries? Computational studies on electronic properties and Li storage capability of Ti_3C_2 and $Ti_3C_2X_2$ (X = F, OH) monolayer, *J. Am. Chem. Soc.*, 2012, **134**, 16909–16916, DOI: 10.1021/ja308463r.

52 C. Eames and M. S. Islam, Ion intercalation into two-dimensional transition-metal carbides: global screening for new high-capacity battery materials, *J. Am. Chem. Soc.*, 2014, **136**, 16270–16276, DOI: 10.1021/ja508154e.

53 N. Lu, L. Li and M. Liu, A review of carrier thermoelectric-transport theory in organic semiconductors, *Phys. Chem. Chem. Phys.*, 2016, **18**(29), 19503–19525.

54 P. Sun, B. Wei, J. Zhang, J. M. Tomczak, A. M. Strydom, M. Søndergaard, B. B. Iversen and F. Steglich, Large Seebeck effect by charge-mobility engineering, *Nat. Commun.*, 2015, **6**(1), 7475.

55 S. Poncé, W. Li, S. Reichardt and F. Giustino, First-principles calculations of charge carrier mobility and conductivity in bulk semiconductors and two-dimensional materials, *Rep. Prog. Phys.*, 2020, **83**(3), 036501.

56 G. Frenking and N. Fröhlich, The nature of the bonding in transition-metal compounds, *Chem. Rev.*, 2000, **100**(2), 717–774.

57 M. M. Mallick and S. Vitta, Giant Enhancement in High-Temperature Thermoelectric Figure-of-Merit of Layered Cobalt Oxide, LiCoO2, Due to a Dual Strategy—Co-Substitution and Lithiation, *Inorg. Chem.*, 2017, **56**(10), 5827–5838.

58 Y. Ohno, D. K. Young, B. A. Beschoten, F. Matsukura, H. Ohno and D. D. Awschalom, Electrical spin injection in a ferromagnetic semiconductor heterostructure, *Nature*, 1999, **402**(6763), 790–792.

59 Y. Zhu, T. Gao, X. Fan, F. Han and C. Wang, Electrochemical techniques for intercalation electrode materials in rechargeable batteries, *Acc. Chem. Res.*, 2017, **50**(4), 1022–1031.

60 C. Eames and M. S. Islam, Ion intercalation into two-dimensional transition-metal carbides: global screening for new high-capacity battery materials, *J. Am. Chem. Soc.*, 2014, **136**(46), 16270–16276.

61 W. Ju, T. Li, X. Su, H. Li, X. Li and D. Ma, Au cluster adsorption on perfect and defective MoS 2 monolayers: structural and electronic properties, *Phys. Chem. Chem. Phys.*, 2017, **19**(31), 20735–20748.

62 H. Naaz, F. P. Malik, A. Mahmood and A. Irfan, Investigation of 2D Nb_3C_2-Based MXenes as the Anode Material for LIBs: A Theoretical Study, *ACS Omega*, 2025, **10**, 5283–5295.

63 L. Wang, W. Liu, F. Bai, X. Zheng, C. Yin, J. Wei, J. Ma, H. Bai and B. Dong, Theoretical study on lithium storage performance of V-doped Ti 2 CO 2 MXene, *RSC Adv.*, 2024, **14**(28), 19945–19952.

64 J. Wang and W. Q. Han, A review of heteroatom doped materials for advanced lithium–sulfur batteries, *Adv. Funct. Mater.*, 2022, **32**(2), 2107166.

65 T. Hiemstra and W. H. Van Riemsdijk, A surface structural approach to ion adsorption: the charge distribution (CD) model, *J. Colloid Interface Sci.*, 1996, **179**(2), 488–508.
66 M. P. Mercer, C. Peng, C. Soares, H. E. Hoster and D. Kramer, Voltage hysteresis during lithiation/delithiation of graphite associated with meta-stable carbon stackings, *J. Mater. Chem. A*, 2021, **9**(1), 492–504.
67 C. Yang, S. Yu, Y. Ma, C. Lin, Z. Xu, H. Zhao, S. Wu, P. Zheng, Z. Z. Zhu, J. Li and N. Wang, Cr3+ and Nb5+ co-doped Ti2Nb10O29 materials for high-performance lithium-ion storage, *J. Power Sources*, 2017, **360**, 470–479.
68 K. E. Prenger, *MXenes and Their Heterostructures with Oxides as Electrodes for Supercapacitors*, Doctoral dissertation, Tulane University, 2022.
69 R. Santoy-Flores, H. N. Fernández-Escamilla, J. I. Páez-Ornelas, E. G. Perez-Tijerina, J. Guerrero-Sánchez, R. Ponce-Pérez, N. Takeuchi and M. G. Moreno-Armenta, Nb2C and Nb2CO2 MXenes as anodes in Li-ion batteries: a comparative study by first-principles calculations, *ACS Omega*, 2024, **9**(26), 28903–28911.